Strain-Engineered Manufacturing of Freeform Carbon Nanotube Microstructures

M. De Volder[1,2,*,†], *S. Park*[3,4,*], *S. Tawfick*[3,4,5], *A.J. Hart*[3,4,†]

[1] *Institute for Manufacturing, University of Cambridge, 17 Charles Babbage Rd, Cambridge, CB3 0FS, UK*

[2] *IMEC, Kapeldreef 75, 3001 Heverlee, Belgium, Department of Mechanical Engineering, Katholieke Universiteit Leuven, 3001 Leuven, Belgium*

[3] *Mechanosynthesis Group, Department of Mechanical Engineering, University of Michigan, 2350 Hayward Street, Ann Arbor, Michigan 48109 USA*

[4] *Mechanosynthesis Group, Department of Mechanical Engineering, Massachusetts Institute of Technology, 77 Massachusetts Ave, Cambridge, Massachusetts, 02139 USA*

[5] *Mechanical Science and Engineering, University of Illinois at Urbana Champaign, Urbana, Illinois, 61822 USA*

**These authors contributed equally.*

[†] *Corresponding authors: M. De Volder: mfld2@cam.ac.uk, A.J. Hart: ajhart@mit.edu*

Abstract

The skins of many plants and animals have intricate micro-scale surface features that give rise to properties such as directed water repellency and adhesion, resistance to fouling, and camouflaging. However, engineered mimicry of these designs has been limited by the capabilities of creating complex forms by top-down fabrication processes. We demonstrate a new technique for scalable manufacturing of freeform microstructures, via strain-engineered growth of aligned carbon nanotubes (CNTs). Lithographic patterning of the CNT growth catalyst is used to locally modulate the CNT growth rate, which causes collective bending during growth with exceptional uniformity. The final shape of the curved CNT microstructures can be approximated via finite element modeling, and compound catalyst shapes produce microstructures with multi-directional curvature and unusual self-organized patterns. Conformal coating of the CNTs enables tuning of the mechanical properties independently from the microstructure geometry, representing a versatile principle for design and manufacturing of complex microstructured surfaces.

Introduction

Scalable fabrication of microstructures that mimic the hierarchical surface designs found in nature has been a long-standing aspiration of material scientists [1-5]. While symbiotic growth of the integrated circuit (IC) and micro electro mechanical systems (MEMS) industries has enabled innovations in 3D fabrication that leverage semiconductor processing tools, these methods, such as interference or inclined exposure lithography are typically limited to arrays of identical structures [6-8]. Rapid prototyping methods such as direct laser writing, multiphoton lithography, and focused ion beam milling can create arbitrary forms but are serial, and therefore have lower areal throughput [9, 10]. It is also especially difficult to fabricate surface structures having curved and/or re-entrant geometries.

On the other hand, use of locally directed actions, such as mechanical stresses, capillary forces, and electromagnetic fields, along with their interactions with templates, offers opportunity to create novel self-organized geometries and to design fabrication processes that achieve attractive combinations of dimensional control and throughput [2, 8, 11-15]. Examples abound in soft materials and chemical systems including micro-scale reaction-diffusion patterns [16, 17], self-assembly of block copolymers [18], and helical aggregation of polymer nanopillars [19, 20]. However, many of these processes need further development to achieve structural uniformity over large substrates.

We present a novel approach taking advantage of microscale top-down lithographic patterning in conjunction with nanoscale self-organization, which enables large-area fabrication of freeform microstructures made of aligned carbon nanotubes (CNTs). This process leverages the influence of the catalyst-substrate interactions on the growth rate of CNTs [21], creating stress gradients during synthesis that guide the CNTs into curved microscale geometries. Our method is analogous to the well-known use of thin film stress to create curved and folded MEMS structures [22]. However, because our process is based on an additive chemical synthesis process instead of a subtractive etching and release technique, it enables the direct synthesis of complex microstructures that are perpendicular rather than parallel to the substrate. This has two major implications: it enables fabrication of closely packed arrays of structures with heterogeneous shapes, and the porosity of the CNT forests enables conformal coating after growth to modify chemical and/or mechanical properties. We demonstrate this latter point by conformal coating of CNT “microtruss” arrays by atomic layer deposition (ALD) and polymer CVD, which increases their mechanical stiffness without changing the geometry.

Results

Fabrication. CNTs grown by chemical vapour deposition (CVD) from a high-density arrangement of catalyst nanoparticles on a substrate are known to self-organize into vertically aligned assemblies often called "CNT forests" [23, 24]. We first observed that the density and rate of CNT forest growth from a widely studied supported catalyst (Fe/Al_2O_3, 1/10 nm) can be influenced by the material immediately beneath the catalyst. This premise is shown in **Fig. 1a**; patterning of CNT growth catalyst (Fe/Al_2O_3) on a SiO_2/TiN "checkerboard" followed by exposure to standard CVD conditions (see Methods) results in a "bi-level" CNT micropillar array. The catalyst patterns directly on SiO_2 grow CNTs to ~100 μm (in < 2 minutes), whereas the patterns on TiN (upon SiO_2) grow CNTs to 50 μm in the same time span. In **Fig. 1b**, "tri-level" CNT forests are grown by arranging patches of catalyst on SiO_2, 70 nm TiN, and 140 nm TiN. This principle could be extended to an arbitrary number of levels or even continuous height gradients via additional lithography and underlayer deposition steps that modulate the growth rate via catalyst-substrate interactions.

Next, we used the above differential growth principle to design compound catalyst/underlayer patterns that directly form curved CNT forest geometries. If a continuous micro-scale catalyst pattern is placed partially on SiO_2 and partially on TiN, the differential growth rates induce stress within the CNT microstructure. For example, as shown in **Fig. 2a and 2b**, a square catalyst pattern with half of its area on the TiN layer bends toward the side which is upon TiN, due to the difference in growth rate on the coupled halves of the structure. The stress is transferred between contacting CNTs at the boundary region via mechanical entanglement and van der Waals interactions among the CNTs. Depending on the curvature and length of the structures, slanted micropillars (**Fig. 2a**), or arches (**Fig. 2b**) can be fabricated. Because the local interaction and differential growth rate determines the trajectory of each structure, large arrays with nearly identical anisotropic shapes can be produced as shown in the SEM images. Importantly, these 3D structures are fabricated using only two standard photolithography steps, one for patterning the TiN layer, and one for patterning the catalyst layer.

The curvature can be controlled by designing the amount of overlap between the catalyst and the TiN underlayer. This is illustrated in **Fig. 3a and b,** which respectively show arrays of round and square cross-section micropillars where the overlap distance is varied from left to right (increments of 5 μm). As expected, the portion of the pillars growing on TiN is always shorter, and as a result, all pillars bend towards the TiN side. As the portion of overlap decreases, the stress induced by the differential growth rate causes increased bending (smaller radius of curvature), reaching a maximum when the catalyst shape is split symmetrically by the TiN layer. With <50% overlap on TiN, the curvature increases gradually until the structure is only slightly curved at the rightmost extent of the array. The CNTs are generally tangential to the curvature of the microstructures, similar to the CNT alignment observed in CNT forests.

Static model of stress-driven CNT curvature. The coupling of stress and CNT growth rate, via the anisotropic mechanics of the CNT forest [25], is a complex problem. However, we find that a static mechanical model analogous to that used for differential expansion of a bi-material cantilever beam can reasonably predict the curvature of CNT structures grown from an overlapped catalyst/TiN rectangle. Starting from the classical formulation of the bimetallic strip model [26], we replace the temperature-dependent expansion term by a differential lengthening term representing the CNT growth rate. Accordingly, the curvature of the compound CNT microstructure is described as:

$$\frac{1}{\rho} = \frac{6\left(\frac{R_1 - R_2}{R_1}\right)(1+m)^2}{w\left(3(1+m)^2+(1+mn)\left(m^2+\frac{1}{mn}\right)\right)} \qquad (1)$$

Here ρ is the radius of curvature, R_1 and R_2 are the growth rates (1 denotes CNTs on Fe/Al_2O_3/SiO_2 and 2 denotes CNTs on Fe//Al_2O_3/TiN), and w is the CNT micropillar width. In addition, *m* and *n* are defined as

$$m = \frac{w_2}{w_1}, n = \frac{E_2}{E_1} \qquad (2)$$

where *w* denotes the width and *E* denotes the respective Young's Moduli of the segments . The value of *n* is specified as 0.6 which is the ratio of the measured areal mass density of CNTs on the respective underlayers; however, because the elongation of each layer is specified in the model, the output is insensitive to this value. The geometric parameters are defined in **Fig. 3c**.

Using the calculated curvatures, and the weighted average growth rate, the shapes of the resultant CNT microstructures were visualized using Matlab. The simulation results correspond to the rows of structures in the SEM image **Fig. 3b**. To compare the experiments to the simulation, the tip position was characterized in horizontal and vertical axes, normalized to the base dimension (*w*) , as shown in **Fig. 3c**. For both the experiment and simulation, the x position of the tip reaches its maximum at 0.4 overlap, and the y position reaches its minimum at approximately 0.6-0.7 overlap.

The differences between the predicted and calculated displacements arise because the model does not capture the exact kinetics of CNT growth, which varies with time. Moreover, it cannot consider how the stress between the two portions of the structure, which are idealized as perfectly coupled without slip, influences the deformation. CNT forests have anisotropic mechanical properties, with the lateral stiffness (perpendicular to the CNT alignment) typically much less than the axial stiffness [27], therefore in principle favoring greater deflection due to built-in stress gradient. Local wrinkling and buckling of the CNTs in the compound microstructures indicates that the growth stress causes complex mechanical deformations, which cannot be predicted by linear elasticity and the bimaterial deflection model (see Fig. 4a).

To gain further insight into the mechanical coupling causing stress-driven bending, we designed a "striped" structure where alternate catalyst/underlayer regions are coupled with a large interfacial area. This structure is symmetric, so it grows straight vertically yet has significant internal stresses. As shown in Fig. 4a and the neighboring insets, the faster growing CNTs deform collectively into a

wavelike pattern. Therefore, while the vertical growth rate of the structure is matched at the interface, the faster growing side still accumulates longer CNTs and these CNTs bend and possibly buckle to accommodate their additional length. This deformation mode is similar to what is observed in mechanically compressed forests [28].

As seen in **Fig. 3a** and supplementary figure **1a**, some structures separate at the interface between the differentially growing regions, due to shear stresses at the interface. In future work, this could be remedied by adapting the structure design to reduce the interfacial shear stress between the segments, or by using a more gradual growth rate gradient to accommodate the stress gradient, such as a three-layer design as in **Fig. 1b**. However, we importantly find that structures that do not separate during synthesis can withstand large subsequent deformations without failure. For instance, supplementary figure **1b** shows an SEM image of an arrangement of bent pillars during compression to 50% vertical strain, at which point delamination at the interface begins only where the pillars kink near their midsection.

CNT and catalyst morphology.

The strain-engineered CNT microstructures show differing CNT density and alignment in the fast and slow growing portions. In **Fig. 4a,b**, the CNTs grown from catalyst on TiN appear to have greater vertical alignment influenced by the interface with the faster-growing region. On the other hand, the CNTs grown from catalyst on SiO_2 are less aligned, due to the retarding force from the slower-growing mating regions.

We hypothesized that the differential CNT growth behavior on the TiN underlayer may be attributed to differences in the catalyst morphology, which can influence the CNT diameter distribution and number density. Atomic Force Microscopy (AFM) showed that as-deposited catalyst layers on SiO_2 and TiN have a similar topology (supplementary figure **2**). However, upon annealing in H_2/He prior to hydrocarbon exposure (see methods), the TiN-catalyst layer forms shallow mounds, tens of nanometers high and hundreds of nanometers wide, in addition to smaller catalyst particles. The control case of catalyst on SiO_2 does not exhibit such topography. For samples with 80 nm TiN layer, the average catalyst particle height and spacing were calculated to be 5.2 nm and 19 nm respectively. Compared to those on SiO_2 (7.5 nm and 18 nm, respectively [29]), the catalyst particle sizes are smaller on average while the spacing is comparable. In addition, the Root Mean Square (RMS) roughness of the annealed catalyst/TiN layer is 5.6 nm, which is considerably higher than that of catalyst on SiO_2 (1.4 nm).

Small Angle X-ray Scattering (SAXS) was used to further investigate the CNT forest morphology [30, 31]. For this experiment, CNTs were grown for 10 minutes on SiO_2, and on 40 nm, and 80 nm TiN layers; these samples reached lengths of 800, 500, and 400 μm respectively. The scattered X-ray intensities were fitted to a mathematical form factor model for hollow cylinders [32] to calculate the

diameter and Herman's orientation parameter, which is a measure of alignment. Both the CNT diameter (**Fig. 4e**) and alignment (supplementary figure **3**) are shown to be lesser for increasing TiN underlayer thickness. Specifically, CNTs on SiO_2 have initial average diameter of 9.5 nm, while CNTs on TiN are approximately 8 nm in diameter. These measurements further support the AFM data which showed that the catalyst particles on TiN layers are smaller than those on SiO_2. The decrease in diameter with growth time has been attributed to diffusion of the catalyst into the Al_2O_3 [30, 33]. The Herman's orientation parameter increases from the top of the forest (the initial growth), then reaches a maximum, and then decreases toward the bottom of the forest. This trend is typically observed for CNT forests grown by CVD, and has been attributed to density variation due to collective activation and deactivation of the growing CNT population [30]. The measured areal mass density of the CNT forests is 0.011 mg mm^{-2} on 80 nm TiN and 0.018 mg mm^{-2} on SiO_2. Therefore, these methods consistency show that placement of the TiN layer under the catalyst results in CNT forests with a smaller average CNT diameter, lesser alignment of CNTs, and a lower density. Although we have not directly compared the mechanical properties of the different segments, we expect that the CNT forests on TiN have lower stiffness, and lesser anisotropy in mechanical properties. The positive correlation between CNT density and alignment is also expected based on recent literature, which demonstrated that CNT-CNT crowding controls alignment within non-patterned forests [34].

Discussion

Complex 3D microstructures

Based on our understanding of the elementary catalyst/underlayer designs that achieve unidirectional bending, we designed a variety of more complex patterns that produce exemplary CNT microstructures having complex curvature. For instance, a compound shape consisting of a "+" catalyst microfeature with each arm offset by a rectangular TiN underlayer results in growth of twisted CNT microstructures (**Fig. 5a**), resembling macroscale propellers. The first-order applicability of the bimaterial bending model discussed above inspired us to evaluate the suitability of finite element modeling (FEM) to predict the shapes of these structures. These were simulated using Comsol FEM software as illustrated in **Fig. 5a,** capturing the uncoupled differential growth rate (**Fig. 1a**) as a 50% expansion mismatch, and estimating the Young's modulus as 30 MPa for the CNTs on TiN and 50 MPa on SiO_2 [35].

Similarly, thin semicircles of CNTs can be directed to curve outward by offsetting the TiN underlayer as shown in **Fig. 5b**. Further structural complexity is shown by the scrolling of thin offset rectangular patterns (**Fig. 5c**). Last, exotic hierarchical arrangements can be formed by the interaction of closely spaced structures, such as the self-organization of offset circular micropillars into wavy

patterns (**Fig. 5d**) that are reminiscent of macroscale crochet stitching. We hypothesize that, after the individual structures bend unidirectionally and contact one another, their continued growth and steric hindrance causes the wavy pattern to form. More investigation is needed to understand the complex deformations of these structures, and their relationship to the mechanics of the CNT forest and the mechanical feedback on the growth process itself.

Notably, in spite of the complex geometries and local deformations, all of these structures can be produced with impressive consistency over large arrays. Arrays of several hundred structures were examined and shown to exhibit nearly identical forms, with defects most frequently arising from debris due to the lithography process rather than the CNT growth step. In this study, we explored structures with critical dimensions as small as 5 μm (**Fig. 5**), and found that the uniformity of the structures was not sacrificed at this scale. We expect that smaller 3D microstructures could be made while still using optical lithography along with high-precision alignment of the catalyst and TiN layers. Notably, sub-micron vertical CNT features have been fabricated for use as interconnects [36]. Further, because the curved and twisted geometries result from collective behavior of CNT forest growth, we expect the structures to require a certain minimal size to average out the stochastic variation of individual CNT growth rate and catalyst lifetime. Considering the approximate CNT-CNT spacing within the current microstructures (~100 nm), the minimal feature size of reliable growth of curved microstructures may be limited to ~1 μm, though this requires further investigation.

Post-processing and mechanical reinforcement

Last, we show that 3D CNT structures can be post-processed via both wet and dry methods that enable tuning of their properties and functionality. Low-density bent CNT micropillars can be transformed into robust densely packed CNT structures by capillary forming (**Fig. 6a-b**) [35, 37, 38]. To do so, the substrate is exposed to a stream of heated acetone vapor, causing acetone to condense onto the CNTs and substrate, and infiltrate each CNT microstructure. Upon subsequent evaporation of the acetone, the CNT forest shrinks laterally, due to the surface tension of the shrinking meniscus. Previously, we showed that capillary forming of vertical CNT microstructures increases the Young's modulus in compression approximately 100-fold, from ~50 MPa to 4 GPa [35]. These values are comparable to soft rubbers and stiff epoxies, respectively. Moreover in the present case the capillary forming process preserves the curved geometry and increases the lateral deflection.

Alternatively, curved CNT microstructures can be coated conformally via vapor phase methods, thereby enabling decoupled control of geometry and mechanical properties. To investigate this, we fabricated CNT "microtruss arrays" (**Fig. 6c-e**), which are analogous to truss designs used in composite materials to achieve high strength and energy absorption at relatively low density [40-42]. The CNT microtrusses each consist of four corner members and a central pillar, meeting at an apex. We explored coating of the CNT microtrusses with both parylene (by chemical vapor deposition, CVD, supplementary figure 4) and alumina (by atomic layer deposition, ALD, **Fig. 6d**). Upon vapor

phase infiltration of the precursors, the CNTs and bundles within the forest are coated individually and conformally [43], enabling fine-tuning of their porosity and mechanics without altering the microstructure geometry. Via flat punch compression testing, we found that a 51 nm Al_2O_3 coating on the CNTs increases the mechanical stiffness by more than 100-fold; typical loading-unloading curves are shown in **Fig. 6e** and supplementary figure 4 for different coating materials and thicknesses. The equivalent stiffness range of the 3D CNT microtrusses is 0.36 to 54 kN m^{-1}, which spans typical values of MEMS springs used in probe card arrays [44]. A further attribute of the TiN underlayer is its electrical conductivity. In the future, electrical integration of strain-engineered CNT structures in conjunction with the post-processing methods described above could be useful in advanced microsystems, including as structural elements or microsensors [45, 46]. Such applications could take advantage of the thermal and mechanical durability of CNTs, as well as the anisotropic properties arising from their alignment and collective curvature.

The ability to fabricate large arrays of 3D microstructures is also conducive to mimicry of nature's advanced functional materials [5]. We say this because the structures shown in Fig. 2 and 5 have similar size and geometry to butterfly wings that have anisotropic wetting properties [47], dry adhesive contacts on the legs of beetles and gecko lizards [3], and microscale sensing hairs found on spiders [39]. Therefore, we suggest that 3D CNT microstructures offer opportunities to further engineer the excellent dry adhesive [48, 53] and superhydrophobic [54] properties previously reported for CNT forests. For mechanical applications such as dry adhesion, an important consideration is the adhesion of the structures to the substrate, as well as the mechanical resilience of the structures upon repeated loading. While we have found that the segments of the curved structures are well adhered to each other (supplementary figure **S1b**), we anticipate that coating or transfer steps may be necessary to anchor the structures for use as robust surface contacts [48]. Exploration of potential optical and photonic applications would require further miniaturization of the structures. Nevertheless, combined with the emerging methods to grow and pattern CNT forests on large-area substrates [49-51], we are optimistic that the methods shown here can enable large-area surface coatings having advanced functionalities.

In summary, we show that strain-engineered CNT growth enables the scalable fabrication of complex 3D microstructures having unidirectional and multidirectional curvature. The capability to produce such structures *en masse* using only 2D patterning methods along with standard thermal processing contrasts the limitations of many existing processes that require serial processing or sequential exposure using complex inclined lithography methods. Moreover, the structures can profit from the mechanical robustness and electrical conductivity of CNTs, and their mechanical and surface properties can be engineered independently from their geometry by conformal coating of the CNTs after growth. This represents a highly attractive principle for materials design, and is promising for scalable manufacturing of 3D microstructured surfaces having biomimetic properties.

Acknowledgements

Financial support to M.D.V was provided by the European Research Council (ERC - HIENA), and the fund for scientific research FWO. Financial support to S.J.P., S.T., and A.J.H. was provided by the Defense Advanced Research Projects Agency (HR0011-10-C-0192) and the Air Force Office of Scientific Research (Young Investigator Program, 11-NA-018). Support from DARPA was received under Agreement to NextGen Aeronautics, and any opinions, findings, and conclusions or recommendations expressed in this material do not necessarily reflect the views of NextGen Aeronautics and/or DARPA. Microfabrication was performed at imec and the Lurie Nanofabrication Facility (LNF), which is a member of the National Nanotechnology Infrastructure Network (NNIN); and electron microscopy was performed at imec and the Michigan Electron Microbeam Analysis Laboratory (EMAL). SAXS measurement was performed at Cornell High Energy Synchrotron Source (CHESS). We thank Mostafa Bedewy for assistance with X-ray scattering measurements and data analysis.

Author Contributions

M.D.V., S.H.T. and A.J.H. conceived the research topic. All authors designed the experiments. M.D.V., S.J.P., and S.H.T. fabricated and characterized the materials. S.J.P. performed simulations. All authors discussed the results, wrote and reviewed the manuscript.

Methods

Substrate patterning and CNT growth

The catalyst and TiN layers are patterned on (100) silicon wafers with 300 nm of thermally grown SiO_2. Each layer is patterned by lift-off processing, by photolithography (photoresist IX845) followed by ultrasonic agitation in acetone. The TiN layer is deposited and patterned first, and then the catalyst layer (1 nm Fe upon 10 nm Al_2O_3) is deposited and patterned. The wafer is then diced into ~1×1 cm pieces, and the substrates are placed in the quartz tube furnace, and the CNT growth is performed. The recipe starts by with flowing 100/400 sccm of He/H_2 while heating to 775 °C over 10 minutes (ramping step); then the system is held at 775 °C for 10 minutes (annealing step) while maintaining the gas flow. Then 100 sccm of C_2H_4 is added to the gas mixture at 775 °C for CNT growth for the desired duration. The typical growth rate is ~50 μm/minute on $Fe/Al_2O_3/SiO_2$. Once the CNTs have grown, C_2H_4 is removed from the gas mixture and the furnace is cooled to <100 °C. After cooling, the system is purged with He before the sample is removed. Optionally, C_2H_4 flow can be maintained while cooling down to improve the adhesion of the CNT microstructures to the substrate. Once the cooling step is complete, the quartz tube is purged with 1000 sccm of He for 5 minutes before opening up the end caps and retrieving the samples.

Small Angle X-ray Scattering (SAXS):

SAXS characterization of CNT microstructures was performed at the Cornell High Energy Synchrotron Source (CHESS) using the G1 beamline (10±0.1 keV, 0.13nm wavelength). The beam is focused to a 10μm spot using a single bounce monocapillary. The CNT sample is placed on a motorized stage and the focused X-ray beam is passed through the sample. The scattered beam is collected using a 2D detector and the measured intensities were normalized to the original intensity measured by another detector at upstream of the CNT sample. The scattering data is then fitted to a mathematical model assuming a log-normal distribution of hollow cylinders to calculate the CNT diameters as well as the Herman's parameter for CNT alignment. The detailed procedure is described by Bedewy et al. [30].

Figure Captions

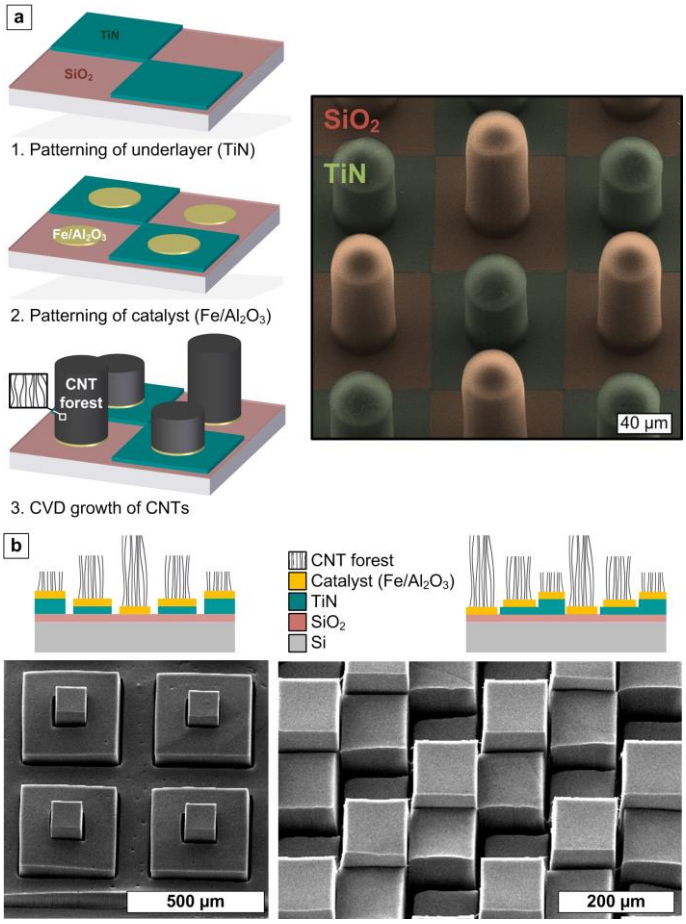

Figure 1. Multi-height CNT micropillar growth using TiN as a rate-controlling catalyst underlayer. (a) Process steps including two lithography steps, and accompanying (color added) pattern of cylindrical CNT micropillars grown on "checkerboard" of alternating TiN (80nm thickness) squares on SiO_2. (b) Triple-height arrays made by substrate and catalyst patterning with three lithography (TiN layers are 40 nm and 80 nm thickness).

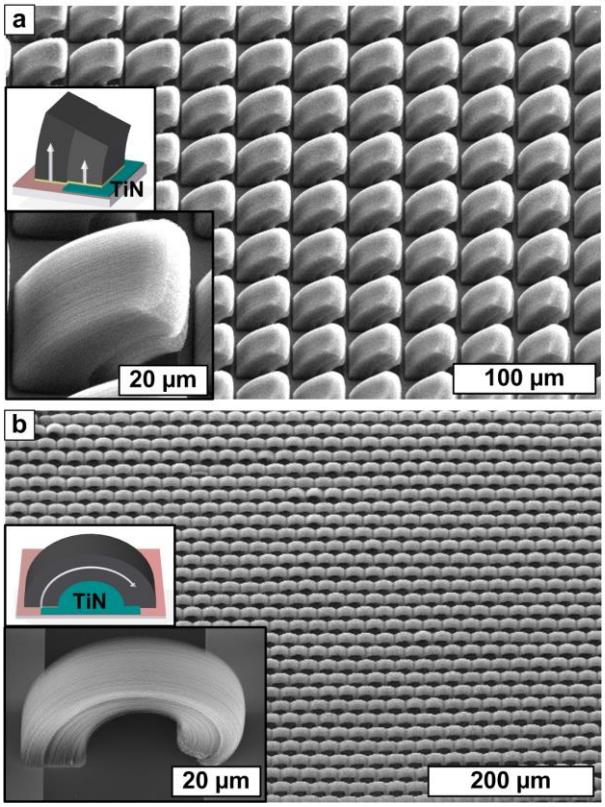

Figure 2. Curved CNT micropillars grown from catalyst rectangles partially overlapping TiN. The pillars bend toward the TiN side, which grows more slowly and couples to the faster-growing region of catalyst directly on SiO_2. (a) Closely-spaced short structures with ~45^o takeoff angle. (b) Arch-like structures that curve over and contact the substrate at their distal ends.

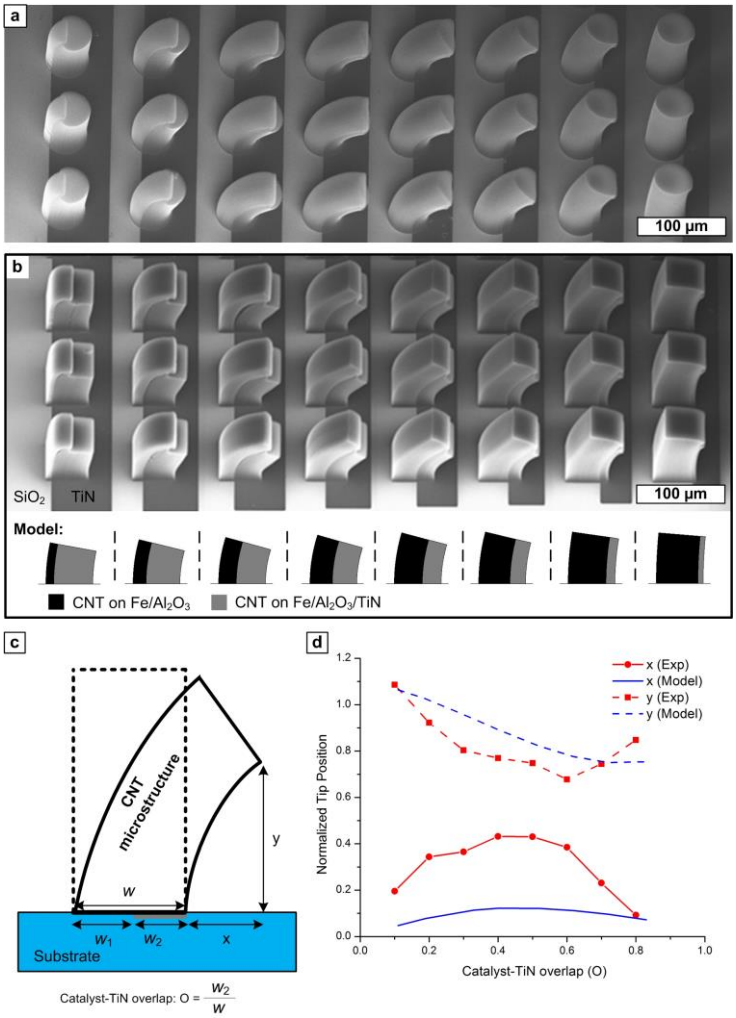

Figure 3. Shape gradients and their use in elementary modeling of the stress-driven CNT growth process. (a,b) arrays of round and square CNT micropillars with decreasing catalyst/TiN overlap from left to right. (c) Schematic of geometric parameters used to quantify deformation of square micropillars. (d) Output of differential expansion model predicting vertical and lateral deflection versus substrate pattern design, comparing simulations, inset to (b), and measurements from SEM images.

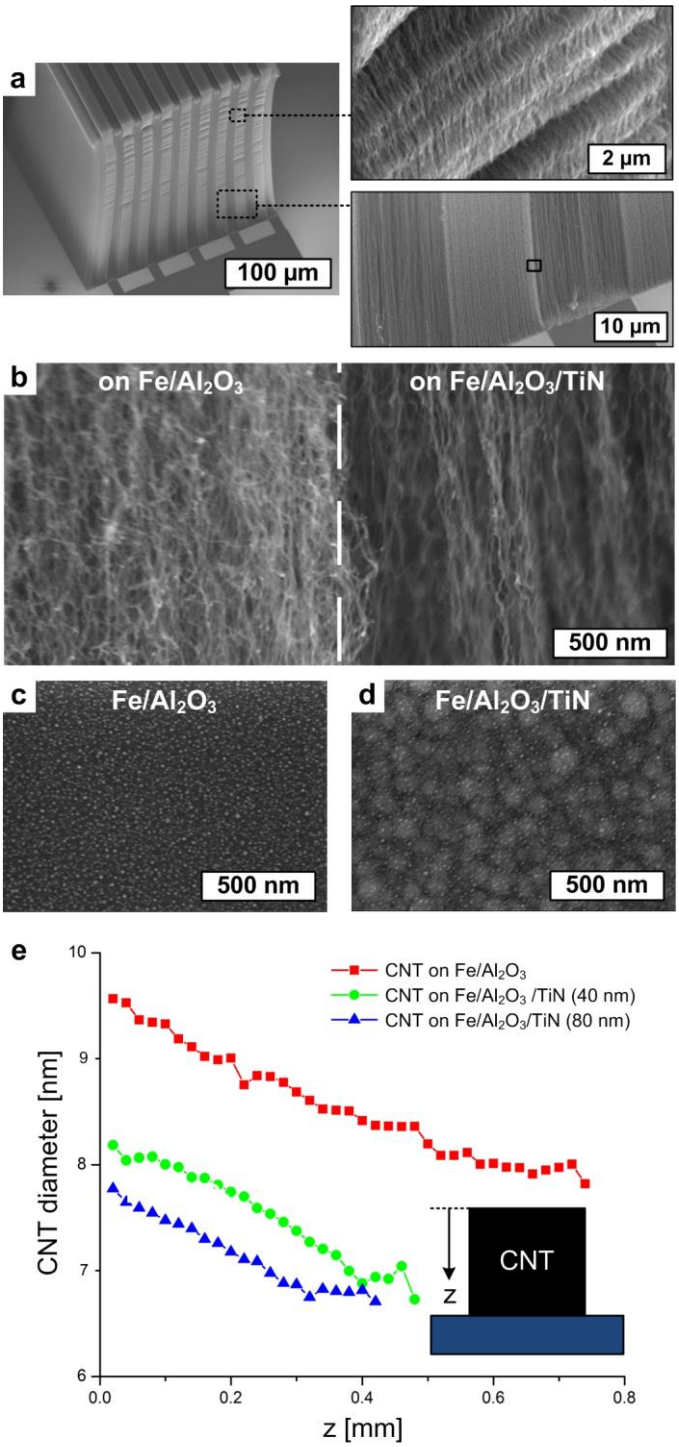

Figure 4. Analysis of CNT morphology. (a) SEM image of micropillar with catalyst on fine stripes of TiN, with close-up images showing the CNT morphology difference and evidence of internal stress causing local deformation. (b) Close-up images of the aligned CNT morphology in adjacent segments of the micropillar. (c,d) SEM images of the substrate morphology after annealing in H_2 and rapid cooling, showing hierarchical morphology of nanoparticles on the catalyst/TiN area. (e) Diameter mapping within the CNT forests, from fitting of SAXS data.

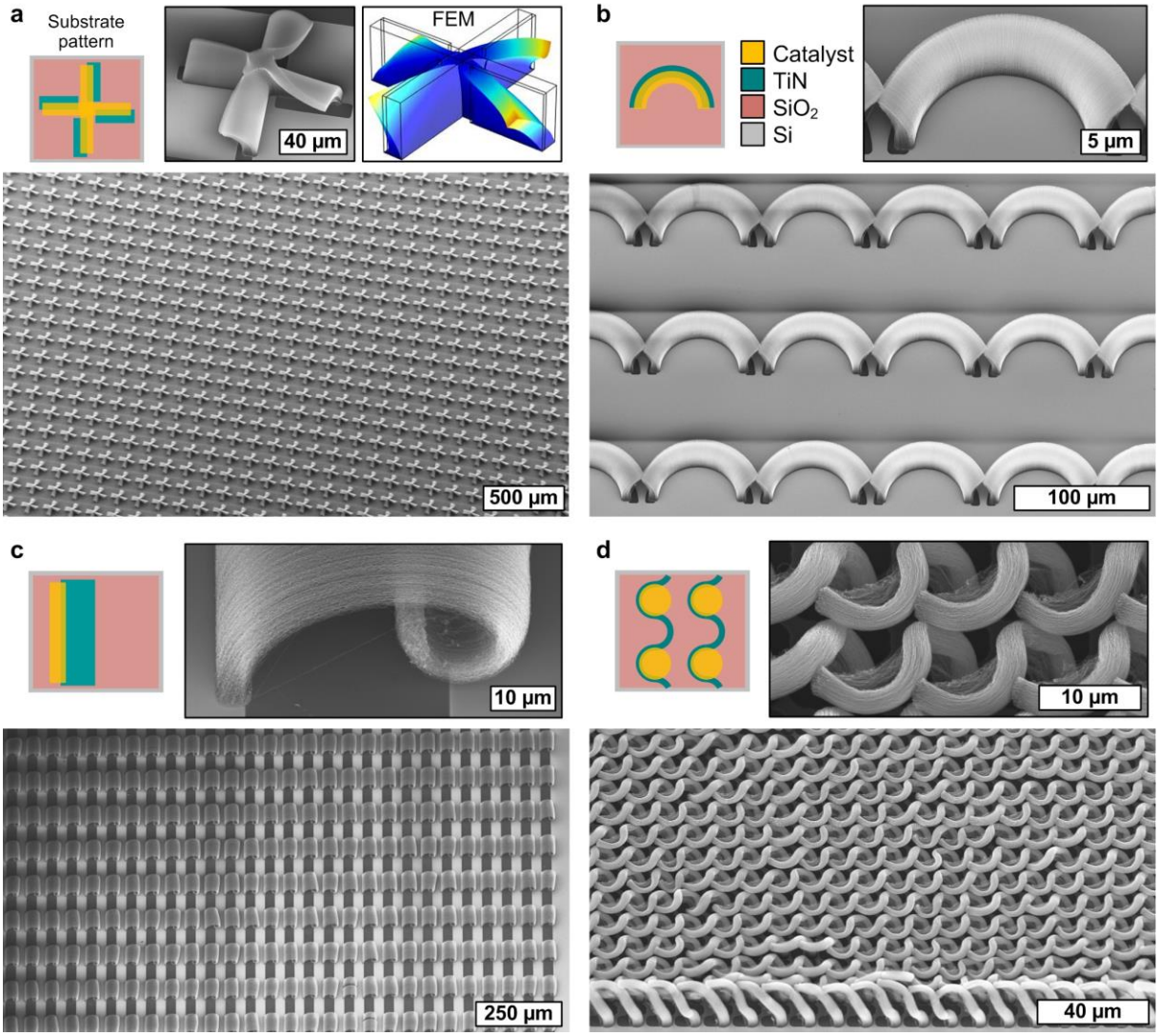

Figure 5. Design and fabrication of arrays of complex microstructures. Each of the four panels contains a sketch (top left) of the catalyst-TiN pattern used for CNT growth, a close-up SEM image (top right), and and an exemplary array of structures (bottom). (a) Twisted propeller-like structures, made from azimuthally offset crosshair catalyst/TiN layers, also compared to finite element model (FEM) prediction of shape (top right). (b) Outward curving semicircles made from radially offset catalyst/TiN layers. (c) Scroll-like deformation of thin-walled microstructures with slight catalyst/TiN overlap. (d) Collective organization of bending microstructures into a wavy pattern.

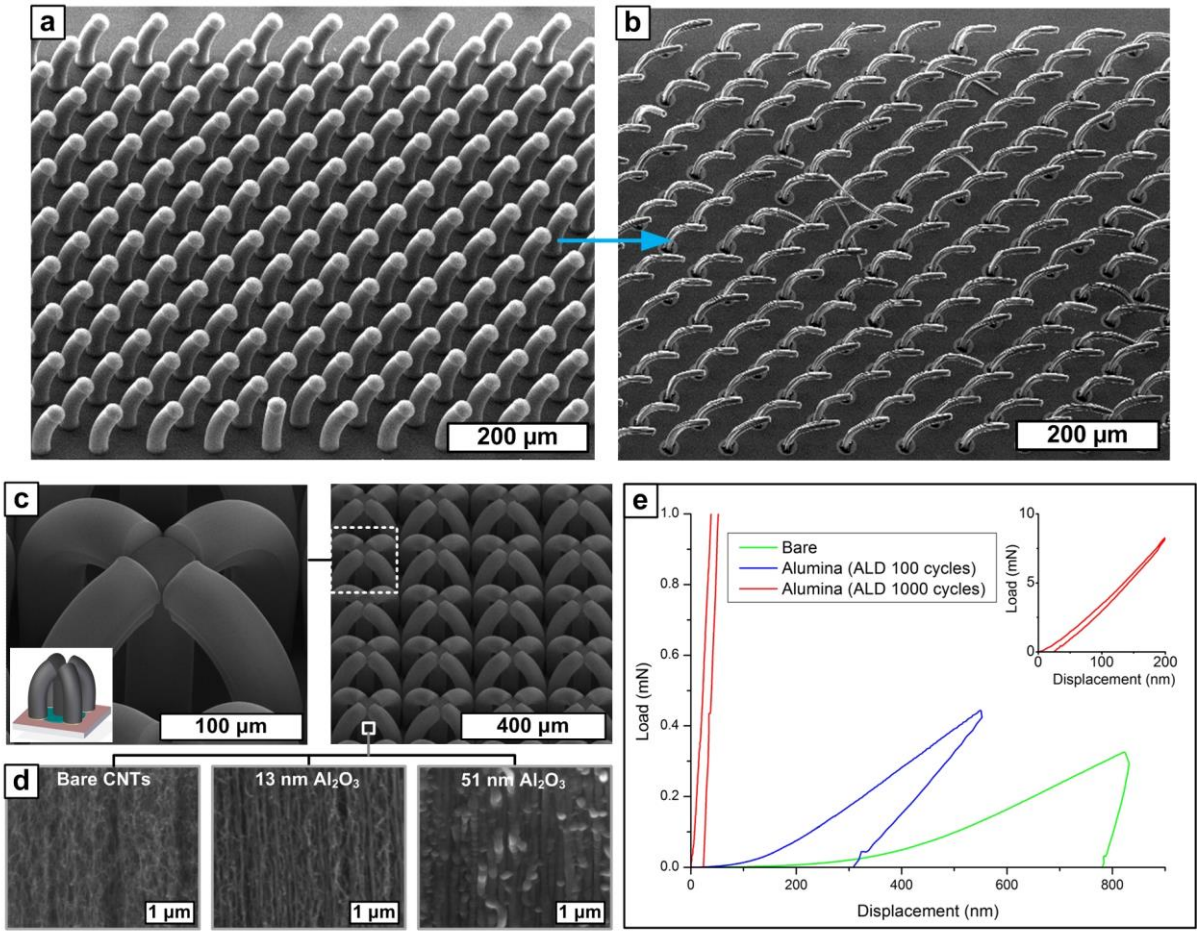

Figure 6. Post-processing of 3DCNT microstructures. (a, b) Array of bending micropillars before and after capillary forming, respectively. The unidirectional anisotropic morphology is maintained and the micropillar cross section decreases, while the lateral deflection angle of the structures increases. (c) Microtruss array fabricated to study mechanical reinforcement by vapor-phase coating of the CNTs. (d) SEM images of aligned CNTs in the forest sidewall before and after coating with Al_2O_3 by ALD. (e) Load-displacement curves before and after ALD coating, where the stiffness is measured from the slope of the unloading curve.

References

1. Aizenberg, J., et al., *Skeleton of Euplectella sp.: Structural hierarchy from the nanoscale to the macroscale.* Science, 2005. **309**(5732).
2. Grinthal, A., et al., *Steering nanofibers: An integrative approach to bio-inspired fiber fabrication and assembly.* Nano Today, 2012. **7**(1): p. 35-52.
3. Arzt, E., S. Gorb, and R. Spolenak, *From micro to nano contacts in biological attachment devices.* Proceedings of the National Academy of Sciences of the United States of America, 2003. **100**(19): p. 10603-10606.
4. Fratzl, P. and R. Weinkamer, *Nature's hierarchical materials.* Progress in Materials Science, 2007. **52**(8): p. 1263-1334.
5. Bae, W.-G., et al., *25th anniversary article: scalable multiscale patterned structures inspired by nature: the role of hierarchy.* Advanced materials (Deerfield Beach, Fla.), 2014. **26**(5): p. 675-700.
6. Campbell, M., et al., *Fabrication of photonic crystals for the visible spectrum by holographic lithography.* Nature, 2000. **404**(6773): p. 53-56.
7. del Campo, A. and C. Greiner, *SU-8: a photoresist for high-aspect-ratio and 3D submicron lithography.* Journal of Micromechanics and Microengineering, 2007. **17**(6): p. R81-R95.
8. Tawfick, S., et al., *Engineering of micro- and nanostructured surfaces with anisotropic geometries and properties.* Advanced materials (Deerfield Beach, Fla.), 2012. **24**(13): p. 1628-74.
9. Bertsch, A., S. Jiguet, and P. Renaud, *Microfabrication of ceramic components by microstereolithography.* Journal of Micromechanics and Microengineering, 2004. **14**(2): p. 197-203.
10. Stampfl, J., et al., *Photopolymers with tunable mechanical properties processed by laser-based high-resolution stereolithography.* Journal of Micromechanics and Microengineering, 2008. **18**(12).
11. Whitesides, G.M. and B. Grzybowski, *Self-assembly at all scales.* Science, 2002. **295**(5564): p. 2418-2421.
12. Grzelczak, M., et al., *Directed Self-Assembly of Nanoparticles.* Acs Nano, 2010. **4**(7): p. 3591-3605.
13. De Volder, M. and A.J. Hart, *Engineering Hierarchical Nanostructures by Elastocapillary Self-Assembly.* Angewandte Chemie-International Edition, 2013. **52**(9): p. 2412-2425.
14. Futaba, D.N., et al., *Dual Porosity Single-Walled Carbon Nanotube Material.* Nano Letters, 2009. **9**(9): p. 3302-3307.
15. De Volder, M.F.L., et al., *Corrugated Carbon Nanotube Microstructures with Geometrically Tunable Compliance.* Acs Nano, 2011. **5**(9): p. 7310-7317.
16. Grzybowski, B.A., et al., *Micro- and nanotechnology via reaction-diffusion.* Soft Matter, 2005. **1**(2): p. 114-128.
17. Noorduin, W.L., et al., *Rationally Designed Complex, Hierarchical Microarchitectures.* Science, 2013. **340**(6134): p. 832-837.
18. Scherer, M.R.J. and U. Steiner, *Efficient Electrochromic Devices Made from 3D Nanotubular Gyroid Networks.* Nano Letters, 2013. **13**(7): p. 3005-3010.
19. Pokroy, B., et al., *Self-Organization of a Mesoscale Bristle into Ordered, Hierarchical Helical Assemblies.* Science, 2009. **323**(5911): p. 237-240.
20. Kang, S.H., et al., *Meniscus Lithography: Evaporation-Induced Self-Organization of Pillar Arrays into Moire Patterns.* Physical Review Letters, 2011. **107**(17).
21. Sam, E.D., et al., *Simultaneous growth of self-patterned carbon nanotube forests with dual height scales.* Nanoscale, 2012. **4**(12): p. 3746-3753.
22. Chalapat, K., et al., *Self-Organized Origami Structures via Ion-Induced Plastic Strain.* Advanced Materials, 2013. **25**(1): p. 91-95.

23. De Volder, M.F.L., et al., *Self-similar organization of arrays of individual carbon nanotubes and carbon nanotube micropillars.* Microelectronic Engineering, 2010. **87**(5-8): p. 1233-1238.
24. Hata, K., et al., *Water-assisted highly efficient synthesis of impurity-free single-waited carbon nanotubes.* Science, 2004. **306**(5700): p. 1362-1364.
25. Maschmann, M.R., et al., *Continuum analysis of carbon nanotube array buckling enabled by anisotropic elastic measurements and modeling.* Carbon, 2014. **66**(0): p. 377-386.
26. Timoshenko, S., *ANALYSIS OF BI-METAL THERMOSTATS.* J. Opt. Soc. Am., 1925. **11**(3): p. 233-255.
27. Maschmann, M.R., et al., *Continuum analysis of carbon nanotube array buckling enabled by anisotropic elastic measurements and modeling.* Carbon, 2014. **66**: p. 377-386.
28. Cao, A.Y., et al., *Super-compressible foamlike carbon nanotube films.* Science, 2005. **310**(5752): p. 1307-1310.
29. Meshot, E.R., et al., *High-Speed in Situ X-ray Scattering of Carbon Nanotube Film Nucleation and Self-Organization.* ACS Nano, 2012. **6**(6): p. 5091-5101.
30. Bedewy, M., et al., *Population Growth Dynamics of Carbon Nanotubes.* ACS Nano, 2011. **5**(11): p. 8974-8989.
31. Wang, B.N., et al., *Quantitative characterization of the morphology of multiwall carbon nanotube films by small-angle X-ray scattering.* Journal of Physical Chemistry C, 2007. **111**(16): p. 5859-5865.
32. Meshot, E.R., et al., *Engineering Vertically Aligned Carbon Nanotube Growth by Decoupled Thermal Treatment of Precursor and Catalyst.* Acs Nano, 2009. **3**(9): p. 2477-2486.
33. Kim, S.M., et al., *Evolution in Catalyst Morphology Leads to Carbon Nanotube Growth Termination.* Journal of Physical Chemistry Letters, 2010. **1**(6): p. 918-922.
34. Xu, M., et al., *Alignment Control of Carbon Nanotube Forest from Random to Nearly Perfectly Aligned by Utilizing the Crowding Effect.* Acs Nano, 2012. **6**(7): p. 5837-5844.
35. De Volder, M.F.L., et al., *Fabrication and electrical integration of robust carbon nanotube micropillars by self-directed elastocapillary densification.* Journal of Micromechanics and Microengineering, 2011. **21**(4).
36. Chiodarelli, N., et al., *Integration and electrical characterization of carbon nanotube via interconnects.* Microelectronic Engineering, 2011. **88**(5): p. 837-843.
37. De Volder, M., et al., *Diverse 3D Microarchitectures Made by Capillary Forming of Carbon Nanotubes.* Advanced Materials, 2010. **22**(39): p. 4384-+.
38. Hayamizu, Y., et al., *Integrated three-dimensional microelectromechanical devices from processable carbon nanotube wafers.* Nature Nanotechnology, 2008. **3**(5): p. 289-294.
39. Barth, F.G., *How to catch the wind: Spider hairs specialized for sensing the movement of air.* Naturwissenschaften, 2000. **87**(2): p. 51-58.
40. Deshpande, V.S., N.A. Fleck, and M.F. Ashby, *Effective properties of the octet-truss lattice material.* Journal of the Mechanics and Physics of Solids, 2001. **49**(8): p. 1747-1769.
41. Radford, D.D., N.A. Fleck, and V.S. Deshpande, *The response of clamped sandwich beams subjected to shock loading.* International Journal of Impact Engineering, 2006. **32**(6): p. 968-987.
42. Gu, S., T.J. Lu, and A.G. Evans, *On the design of two-dimensional cellular metals for combined heat dissipation and structural load capacity.* International Journal of Heat and Mass Transfer, 2001. **44**(11): p. 2163-2175.
43. TAWFICK, S., et al., *Nanocomposite microstructures with tunable mechanical and chemical properties.* PHYSICAL CHEMISTRY CHEMICAL PHYSICS, 2010. **12**(17): p. 4446-4451.
44. Novitsky, J. and C. Miller, *Wafer-level CSP, wafer-level assembly/test: Integrating backend processes.* Solid State Technology, 2001. **44**(2): p. 78-+.
45. De Volder, M., et al., *Hydrogel-driven carbon nanotube microtransducers.* Soft Matter, 2011. **7**(21): p. 9844-9847.
46. Hutchison, D.N., et al., *Carbon Nanotubes as a Framework for High-Aspect-Ratio MEMS Fabrication.* Journal of Microelectromechanical Systems, 2010. **19**(1): p. 75-82.

47. Zheng, Y., X. Gao, and L. Jiang, *Directional adhesion of superhydrophobic butterfly wings.* Soft Matter, 2007. **3**(2): p. 178-182.
48. Rong, Z., et al., *Bio-Inspired Hierarchical Polymer Fiber-Carbon Nanotube Adhesives.* Advanced Materials, 2014. **26**(9): p. 1456-1461.
49. Yasuda, S., et al., *Improved and Large Area Single-Walled Carbon Nanotube Forest Growth by Controlling the Gas Flow Direction.* Acs Nano, 2009. **3**(12): p. 4164-4170.
50. Zhang, Q., et al., *Carbon Nanotube Mass Production: Principles and Processes.* Chemsuschem, 2011. **4**(7): p. 864-889.
51. Polsen, E.S., A.G. Stevens, and A.J. Hart, *Laser Printing of Nanoparticle Toner Enables Digital Control of Micropatterned Carbon Nanotube Growth.* Acs Applied Materials & Interfaces, 2013. **5**(9): p. 3656-3662.
52. Mizuno, K., et al., *A black body absorber from vertically aligned single-walled carbon nanotubes.* Proceedings of the National Academy of Sciences of the United States of America, 2009. **106**(15): p. 6044-6047.
53. Qu, L., et al., *Carbon nanotube arrays with strong shear binding-on and easy normal lifting-off.* Science, 2008. **322**(5899): p. 238-242.
54. Lau, K.K.S., et al., *Superhydrophobic carbon nanotube forests.* Nano Letters, 2003. **3**(12): p. 1701-1705.